Journal of Industrial and Management Optimization

https://www.aimspress.com/journal/jimo

JIMO, 22(4): 1824–1846.
DOI:10.3934/jimo.2026067
Received: 20 January 2026
Revised: 01 March 2026
Accepted: 04 March 2026
Published: 12 March 2026

Research article

A physics-informed neural network framework for ice-water two-phase temperature reconstruction and interface inversion in Arctic sea ice

Yang Liu[1,2], Lei Wang[1,*], BingYan Gao[2], XueLing Yi[1], Peng Lu[2] and Xu Zhang[1]

[1] School of Mathematical Science, Dalian University of Technology, Dalian, 116000, China

[2] State Key Laboratory of Coastal and Offshore Engineering, Dalian University of Technology, Dalian, 116000, China

* **Correspondence:** Email: wanglei@dlut.edu.cn.

Abstract: Accurate characterization of temperature fields and ice thickness evolution is critical for the rapidly changing Arctic sea ice system, when field-based buoy observations remain limited. Building on weak solution theory and solvability analysis for the coupled ice-water two-phase system, a physics-informed neural network (PINN) framework was developed for forward simulation and interface inversion of a Stefan free-boundary problem. The proposed approach enabled the simultaneous reconstruction of temperature fields in phases and identification of the interface trajectory. Methodologically, the framework combined rigorous theoretical analysis, a PINN implementation consistent with physical constraints, and observation-driven validation, thereby providing a systematic procedure for temperature field reconstruction and physically consistent inversion in ice-water two-phase Stefan free-boundary inverse problems. Validation proceeded from equivalent-flux benchmarks to fully coupled two-phase simulations. In the equivalent-flux stage, the water-phase impact on the ice was parameterized by a time-varying equivalent oceanic heat flux. With a three-stage training strategy and a multiplicative correction factor for the conductive flux, the ice temperature error was below 0.5 °C, and the absolute thickness error was under 2.5 cm. In the coupled stage, hard enforcement of the boundary conditions further stabilized convergence, keeping temperature errors below 0.3 °C in both phases and limiting the absolute thickness error to at most 4 cm. These results demonstrated that a physics-constrained PINN can deliver stable and accurate two-phase thermodynamic inversion from limited observations, and they motivate extensions toward a unified atmosphere-snow-ice-ocean inversion framework.

Keywords: Arctic sea ice; physics-informed neural networks (PINNs); two-phase heat transfer; Stefan interface; interface inversion

Mathematics Subject Classification: 86A05, 65M32, 68T07

1. Introduction

Under global warming, Arctic temperatures are increasing at a rate well above the global mean. This Arctic amplification is reshaping the polar climate system [1, 2]. Arctic sea ice constitutes a key interface between the atmosphere and the ocean, regulating the regional energy budget through albedo feedback and air-sea heat exchange while also influencing atmospheric circulation and ecosystem dynamics [3, 4]. Continued warming has accelerated the decline in sea ice extent and thickness [5, 6]. As a result, the Arctic is shifting from a multi-year ice regime to a "new Arctic" dominated by first-year ice, characterized by stronger seasonality and increased variability [7, 8]. The 2019–2020 Multidisciplinary drifting Observatory for the Study of Arctic Climate (MOSAiC) highlighted the central role of thermodynamic processes in the sea ice mass balance [9, 10]. Therefore, accurately resolving the spatiotemporal evolution of the coupled ice-water temperature fields and sea ice thickness is essential to characterize the sea ice heat budget and its response to atmospheric and oceanic forcing [11, 12].

Current estimates of ice-water temperature fields and ice thickness mostly rely on field observations, satellite remote sensing, and numerical modeling [13, 14]. Field observations provide local temperature profiles and thickness at high temporal resolution, but they have limited spatial coverage and are susceptible to missing data, noise, and instrument drift [15]. Satellite remote sensing provides large-scale information on sea-ice state variables, but retrievals are sensitive to input assumptions such as snow depth and surface roughness [16, 17], and systematic differences persist among data sources and retrieval algorithms [18, 19]. Numerical modeling can generate continuous spatiotemporal fields [20, 21], but the results depend on thermophysical parameterizations, descriptions of snow and ice layer structure, and ocean-side heat exchange [22, 23], which are coupled nonlinearly through interfacial phase change conditions and therefore remain highly sensitive to boundary and parameter perturbations [24]. With sparse observations and uncertain boundary forcing, simultaneous reconstruction of the two-phase temperature fields and identification of ice-water interface trajectory pose a strongly nonlinear inverse problem [25]. The main challenge is that Stefan coupling tightly binds the two-phase states to the moving boundary, thereby amplifying the impact of observational perturbations on the inversion [26].

Physics-informed neural networks (PINNs) provide a promising framework for this class of problems. In PINNs, the unknown temperature fields and the interface trajectory are represented as differentiable neural-network surrogates. The governing equations, boundary conditions, and interface conditions are encoded as residual terms in the loss function, and automatic differentiation enables a mesh-free scheme for both solution and identification [27]. For the ice-water two-phase Stefan inverse problem considered here, PINNs can enforce interfacial coupling constraints directly in continuous space and time while assimilating irregularly sampled observations of ice-water temperature and thickness in an end-to-end manner [28]. This enables simultaneous reconstruction of the state fields and the free boundary. Compared with traditional PDE-constrained optimization, PINNs avoid an explicit forward solve at each iteration and eliminate repeated remeshing with consistency enforcement under a moving boundary [29, 30]. This yields greater implementation flexibility [31]. In recent years, PINN research has moved beyond basic residual minimization [27] toward systematic improvements in stability, conservation, and structure preservation [32]. Related efforts address training ill-conditioning and loss imbalance [33], domain decomposition with coupling and flux consistency [34], and structured enforcement of boundary conditions [35]. Studies further suggest that, for complex PDE-constrained problems, the central challenge lies not only in function approximation but also in the numerical

realization of constraint structure and the design of effective optimization pathways [36]. Although PINNs have shown potential for Stefan-type problems [37], a unified treatment of property contrasts across the interface and interface-trajectory identification, and training stability remains underdeveloped.

Against this background, we examine an ice-water two-phase Stefan free-boundary inverse problem and seek to establish a unified framework that integrates continuous theoretical analysis, a PINN implementation consistent with physical constraints, and observation-driven validation. Building on existence results for weak solutions and the associated identification problem, a PINN-based solution and inversion methodology is developed that respects the interfacial closure structure, and its stability and physical consistency are assessed using Arctic sea-ice observations. We do not include a quantitative baseline comparison with conventional numerical Stefan solvers or data assimilation methods. The rationale is that the primary objective is a unified implementation of two-phase temperature-field reconstruction, interface-trajectory inversion, and interfacial flux closure under limited observations. The resulting objective and constraint structure are not directly aligned with standard forward simulations or conventional assimilation formulations. Accordingly, the emphasis is on establishing a physics-constrained PINN framework supported by continuous theory, rather than on an empirical ranking of numerical paradigms.

This paper is organized as follows: In Section 2, we introduce the governing equations, boundary conditions, and Stefan interface conditions for the ice–water two-phase heat-conduction system, and then formulate the interface-trajectory identification problem along with the associated PINN framework. In Section 3, the training strategy and experimental design are described, followed by the presentation and discussion of the numerical results. We conclude in Section 4 with a summary of the major findings.

2. Models and methods

In this section, we cover the continuous model analysis and the construction of the physics-informed network framework, but the two are not presented in parallel. Instead, the PINN formulation follows directly from the continuous analysis in a clear progression. The aim of the continuous analysis is to define, within a functional analytic setting, an appropriate notion of solution for the coupled ice-water two-phase system and to establish existence and stability results. This clarifies the continuous object of interest and its associated constraint structure for the remainder of the paper. Building on this structure, the physics-informed neural network formulation converts the governing equations, boundary conditions, and interfacial closure relations into a differentiable approximation problem over a neural-network parameterized function class. Accordingly, the section is organized along a progression from continuous theory to numerical implementation, with the analysis providing the basis for well-posedness and the PINN framework providing a structure-consistent parameterization and computational realization.

2.1. Ice-water two-phase heat conduction model

The Arctic sea ice thermodynamic system considered is a coupled ice layer and underlying ocean water (Figure 1). It is referred to as an ice-water two-phase system, and only one-dimensional thermodynamics in the vertical direction are considered.

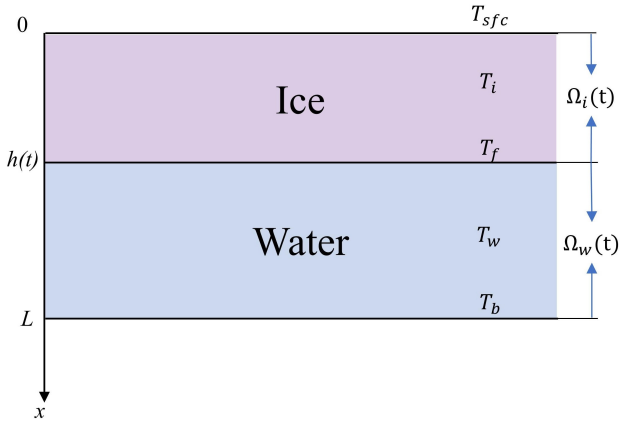

Figure 1. Ice-water two-phase system.

Let $t_f > 0$ and the total fixed depth of the ice-water column be $L > 0$. A vertical coordinate x is introduced, positive downward, with the ice surface at $x = 0$. The ice-water interface is at $x = h(t) \in (0, L)$. The phase domains are defined by

$$\Omega_i(t) = (0, h(t)), \quad \Omega_w(t) = (h(t), L), \quad t \in (0, T).$$

Let $T_i(x, t)$ and $T_w(x, t)$ denote the temperatures in the ice and water phases, respectively. For each phase $\ell \in \{i, w\}$, ρ_ℓ, c_ℓ, and $k_\ell > 0$ denote the density, specific heat, and thermal conductivity, and q_ℓ denotes volumetric heat source. For a given interface trajectory $h(\cdot)$, the phase temperatures satisfy the parabolic heat equations

$$\rho_i c_i \partial_t T_i = \partial_x (k_i \partial_x T_i) + q_i(x, t), \quad (x, t) \in \Omega_i(t) \times (0, t_f), \tag{1a}$$
$$\rho_w c_w \partial_t T_w = \partial_x (k_w \partial_x T_w) + q_w(x, t), \quad (x, t) \in \Omega_w(t) \times (0, t_f). \tag{1b}$$

The initial conditions are

$$T_i(x, 0) = T_{i0}(x), \qquad x \in (0, h_0), h_0 = h(0), \tag{2a}$$
$$T_w(x, 0) = T_{w0}(x), \qquad x \in (h_0, L). \tag{2b}$$

The boundary and interface conditions are given by

$$T_i(0, t) = T_{\text{sfc}}(t), \quad T_w(L, t) = T_b(t), \qquad t \in (0, t_f), \tag{3a}$$
$$T_i(h(t), t) = T_w(h(t), t) = T_f(t), \qquad t \in (0, t_f). \tag{3b}$$

To avoid degeneration of the spatial domains, constants $0 < h_{\min} < h_{\max} < L$ are prescribed, and the initial interface position is taken as $h_0 \in [h_{\min}, h_{\max}]$. The admissible set is defined by

$$U_{ad} := \left\{ h \in H^1(0, t_f) \mid h_{\min} \le h(t) \le h_{\max} \text{ a.e. } h(0) = h_0 \right\}.$$

For any fixed $h \in U_{ad}$, the time-dependent physical domains are mapped onto the fixed reference interval $(0, 1)$. Separate coordinate transformations are introduced for the ice and water phases. Specifically,

for $\zeta \in (0,1)$, the ice phase is parameterized by $x = h(t)\zeta$, and the water phase is parameterized by $x = h(t) + (L - h(t))\zeta$. The transformed temperature fields are defined as

$$\widetilde{T}_i(\zeta,t) = T_i(h(t)\zeta,t), \quad \widetilde{T}_w(\zeta,t) = T_w(h(t) + (L-h(t))\zeta,t),$$

and the corresponding transformed volumetric heat sources are given by

$$\tilde{q}_i(\zeta,t) = q_i(h(t)\zeta,t), \quad \tilde{q}_w(\zeta,t) = q_w(h(t) + (L-h(t))\zeta,t).$$

This transformation preserves the constraint structure of the original problem. It also absorbs the uncertainty introduced by geometric evolution into the equation coefficients and lower-order terms, enabling a weak formulation on a fixed domain and facilitating the subsequent a priori estimates and limit arguments.

To further homogenize the boundary conditions, affine lifting functions are introduced in the ice and water phases,

$$\tilde{\eta}_i(\zeta,t) = T_{\mathrm{sfc}}(t) + \zeta(T_f(t) - T_{\mathrm{sfc}}(t)), \quad \tilde{\eta}_w(\zeta,t) = T_f(t) + \zeta(T_b(t) - T_f(t)).$$

Define

$$\tilde{y}_i(\zeta,t) = \widetilde{T}_i(\zeta,t) - \tilde{\eta}_i(\zeta,t), \quad \tilde{y}_w(\zeta,t) = \widetilde{T}_w(\zeta,t) - \tilde{\eta}_w(\zeta,t),$$

then the boundary conditions in Eq. (3) are equivalent to the homogeneous Dirichlet conditions

$$\tilde{y}_i(0,t) = \tilde{y}_i(1,t) = 0, \quad \tilde{y}_w(0,t) = \tilde{y}_w(1,t) = 0, \quad t \in (0,t_f). \tag{4}$$

As a result, the choice of function spaces in the weak formulation becomes more natural, and the treatment of boundary terms in the energy estimates is simplified, which facilitates the existence and stability analysis. Moreover, assume that ρ_ℓ, c_ℓ, and k_ℓ are positive constants for $\ell \in \{i,w\}$. The system in Eq. (1) is then equivalent to

$$\partial_t \tilde{y}_i - \frac{h'(t)}{h(t)}\zeta\partial_\zeta \tilde{y}_i = \frac{\alpha_i}{h(t)^2}\partial_{\zeta\zeta}\tilde{y}_i + f_i(\zeta,t;h), \tag{5a}$$

$$\partial_t \tilde{y}_w + \frac{h'(t)}{L-h(t)}(\zeta-1)\partial_\zeta \tilde{y}_w = \frac{\alpha_w}{(L-h(t))^2}\partial_{\zeta\zeta}\tilde{y}_w + f_w(\zeta,t;h), \tag{5b}$$

for $(\zeta,t) \in (0,1)\times(0,t_f)$, where $\alpha_i = k_i/(\rho_i c_i)$ and $\alpha_w = k_w/(\rho_w c_w)$. The source terms can be written as

$$f_i(\zeta,t,h) = \frac{1}{\rho_i c_i}\tilde{q}_i(\zeta,t) - T'_{\mathrm{sfc}}(t) - \zeta(T'_f(t) - T'_{\mathrm{sfc}}(t)) + \frac{h'(t)}{h(t)}\zeta(T_f(t) - T_{\mathrm{sfc}}(t)),$$

$$f_w(\zeta,t,h) = \frac{1}{\rho_w c_w}\tilde{q}_w(\zeta,t) - T'_f(t) - \zeta(T'_b(t) - T'_f(t)) - \frac{h'(t)}{L-h(t)}(\zeta-1)(T_b(t) - T_f(t)).$$

The initial condition in Eq. (2) becomes

$$\tilde{y}_i(\zeta,0) = T_{i0}(h_0\zeta) - \tilde{\eta}_i(\zeta,0), \quad \tilde{y}_w(\zeta,0) = T_{w0}(h_0 + (L-h_0)\zeta) - \tilde{\eta}_w(\zeta,0). \tag{6}$$

Let $V = H_0^1(0,1)$ and $H = L^2(0,1)$. The embedding $V \hookrightarrow H$ is continuous and dense. By the Riesz representation theorem [38], $H \equiv H^*$. This yields the Gelfand triple $V \hookrightarrow H \equiv H^* \hookrightarrow V^*$. The purpose

of introducing this structure is to obtain a consistent weak formulation for the coupled parabolic system when the time derivative is defined only in a dual-space sense, and to provide a unified framework for the variational formulation, energy estimates, and compactness arguments that follow. For each $\ell \in \{i, w\}$, define the time-dependent bilinear form

$$a_\ell(t; h; u, v) = \int_0^1 \frac{\alpha_\ell}{\gamma_\ell(t; h)^2} u_\zeta v_\zeta \, d\zeta - \int_0^1 b_\ell(\zeta, t; h) u_\zeta v \, d\zeta, \quad u, v \in V, \tag{7}$$

where $\gamma_i(t) = h(t)$, $b_i(\zeta, t) = \frac{h'(t)}{h(t)}\zeta$, $\gamma_w(t) = L - h(t)$, and $b_w(\zeta, t) = -\frac{h'(t)}{L-h(t)}(1-\zeta)$.

Definition 2.1 (Weak solution)**.** Fix $h \in U_{ad}$. A pair $(\tilde{y}_i, \tilde{y}_w)$ is called a weak solution of Eq. (5) if, for each $\ell \in \{i, w\}$,

$$\tilde{y}_\ell \in L^2(0, T; V) \cap C([0, t_f]; H), \ \partial_t \tilde{y}_\ell \in L^2(0, t_f; V^*),$$

and, for almost every $t \in (0, t_f)$ and every $v \in V$,

$$\langle \tilde{y}'_\ell(t), v \rangle_{V^*,V} + a_\ell(t; h; \tilde{y}_\ell(t), v) = \int_0^1 f_\ell(\zeta, t; h) v(\zeta) \, d\zeta,$$

with the initial condition given by Eq. (6).

The bounds $h_{\min} \le h \le h_{\max}$ imply uniform ellipticity of the diffusion part in Eq. (9), since the coefficients $\frac{\alpha_\ell}{\gamma_\ell(t;h)^2}$ are uniformly positive and uniformly bounded in time. The transport part is of lower order because it involves only first derivatives. Moreover, $h \in H^1(0, t_f)$ ensures that the transport coefficients $b_\ell(\zeta, t; h)$ are controlled in times. As a result, the bilinear forms satisfy a uniform Gårding type lower bound of the form [39]

$$a(t; u, u) \ge c_0 \|u\|_V^2 - C_0 \|u\|_H^2, \quad u \in V,$$

where $c_0 > 0$ and $C_0 \ge 0$ are independent of t and depend only on $h_{\min}$, $h_{\max}$, L, and the physical parameters. Standard variational well-posedness results for linear parabolic evolution equations then yield existence, uniqueness, and a prior energy estimates.

Theorem 2.2. *Let $h \in U_{ad}$. Assume $\tilde{q}_i, \tilde{q}_w \in L^2(0, t_f; H)$, $T_{sfc}, T_f, T_b \in H^1(0, t_f)$, $\tilde{y}_i(\cdot, 0) \in H$, and $\tilde{y}_w(\cdot, 0) \in H$. Then the weak solution in Definition 2.1 exists and is unique. In addition, it satisfies the uniform energy estimate*

$$\sup_{t\in[0,T]} \|\tilde{y}_\ell(t)\|_H^2 + \int_0^T \|\tilde{y}_\ell(t)\|_V^2 dt \le C \left(\|\tilde{y}_\ell(\cdot, 0)\|_H^2 + \int_0^T \|f_\ell(\cdot, t; h)\|_{V^*}^2 dt \right), \ \ell \in \{i, w\},$$

where $C > 0$ depend only on $h_{\min}$, $h_{\max}$, L, and the physical parameters.

The inverse coordinate transformation and the inverse homogenization map uniquely recover (T_i, T_w) from $(\tilde{y}_i, \tilde{y}_w)$. This defines the forward solution operator

$$\mathcal{S} : U_{\text{ad}} \to L^2((0, L) \times (0, T))^2, \quad \mathcal{S}(h) = (T_i(\cdot, \cdot; h), T_w(\cdot, \cdot; h)).$$

According to [40], if h_n and $h \in U_{ad}$ satisfy $h_n \to h$ in $C([0, t_f])$ and $\sup_n \|h'_n\|_{L^2(0,T)} < \infty$, then

$$\|\mathcal{S}(h_n) - \mathcal{S}(h)\|_{L^2((0,L)\times(0,t_f))} \to 0.$$

Therefore, the mapping $h \mapsto T(\cdot, \cdot; h)$ is strongly continuous on U_{ad}.

To close the two-phase system at the ice-water interface, temperature continuity at the interface given by Eq. (3b), is not sufficient. An additional energy balance must be imposed in the form of a Stefan condition. This condition states that the interfacial melting or freezing rate is determined jointly by the conductive heat flux from the ice side and the heat flux from the water side. At the interface $x = h(t)$, the conductive heat flux on the ice side is defined as

$$F_c(h)(t) = -k_i \partial_x T_i(h(t)^-, t; h), \quad t \in (0, t_f). \tag{8}$$

The heat flux on the water side is treated as a prescribed function $F_w \in L^2(0, T)$, which may depend on the water temperature. The Stefan closure condition then reads

$$\rho_i L_f h'(t) = F_c(h)(t) - F_w(t), \quad t \in (0, t_f), \quad h(0) = h_0, \tag{9}$$

where $L_f > 0$ denotes the latent heat of fusion. Using the fixed-domain transformation together with the homogenization transformation, the flux expression in Eq. (8) can be rewritten as

$$F_c(h)(t) = -\frac{k_i}{h(t)} \partial_\zeta \widetilde{T}_i(1, t; h) = -\frac{k_i}{h(t)} \left(\partial_\zeta \tilde{y}_i(1, t; h) + T_f(t) - T_{\text{sfc}}(t) \right). \tag{10}$$

2.2. Identification model for the ice-water interface trajectory $h(\cdot)$

Let the observed temperature field satisfy $T_{\text{Obs}} \in L^2((0, L) \times (0, t_f))$. For any $h \in U_{ad}$ and $(x, t) \in (0, L) \times (0, t_f)$, the temperature field of the coupled ice-water system is represented by

$$T(x, t; h) = \mathbf{1}_{(0,h(t))}(x) T_i(x, t; h) + \mathbf{1}_{(h(t),L)}(x) T_w(x, t; h), \tag{11}$$

where $\mathbf{1}_{(0,h(t))}(x)$ denotes the indicator function, taking the value 1 when $x \in (0, h(t))$ and 0 otherwise. Fix a regularization parameter $\lambda > 0$. The objective functional is defined by

$$\begin{aligned} J(h) &= J_{\text{data}}(h) + \lambda J_{\text{reg}}(h), \\ &= \frac{1}{2} \int_0^{t_f} \int_0^L |T(x, t; h) - T_{\text{Obs}}(x, t)|^2 \, dx dt + \frac{1}{2} \int_0^{t_f} |h'(t)|^2 \, dt. \end{aligned}$$

The identification of the interface trajectory is formulated as the following minimization problem over the admissible set U_{ad}:

$$\min_{h \in U_{\text{ad}}} J(h). \tag{12}$$

To ensure well-posedness of problem Eq. (12), an existence result for the minimizer is stated below, together with a brief proof.

Theorem 2.3 (Existence of an optimal interface trajectory)**.** *There exists $h^* \in U_{ad}$ such that*

$$J(h^*) = \inf_{h \in U_{ad}} J(h).$$

Equivalently, the minimization problem Eq. (11) admits at least one minimizer in U_{ad}.

Proof. Let $\{h_n\} \subset U_{ad}$ be a minimizing sequence such that $J(h_n) \downarrow \inf_{U_{ad}} J(h)$. Because of the presence of the regularization term J_{reg}, the sequence $\{h_n\}$ is bounded in $H^1(0, t_f)$. By weak compactness in Hilbert spaces, there exist a subsequence $\{h_{n_k}\}$ and a limit $h^* \in H^1(0, t_f)$, such that

$$h_{n_k} \rightharpoonup h^*, \qquad \text{in } H^1(0, t_f).$$

Moreover, the compact embedding $H^1(0, t_f) \hookrightarrow C([0, t_f])$ implies [38]

$$h_{n_k} \to h^*, \qquad \text{in } C([0, t_f]).$$

The admissible set U_{ad} is closed with respect to this convergence; hence, $h^* \in U_{ad}$. By the strong continuity of the solution mapping $\mathcal{S}$, it follows that $J_{\text{data}}(h_{n_k}) \to J_{\text{data}}(h^*)$. On the other hand, the map $h \to \int_0^T |h'(t)|^2 dt$ is weakly lower semi-continuous in $H^1(0, t_f)$ [41]. Therefore,

$$J(h^*) \le \liminf_{k\to\infty} J(h_{n_k}) = \inf_{h\in U_{ad}} J(h).$$

Consequently, h^* is an optimal solution of Eq. (12) □

To establish existence for the coupled system consisting of the two-phase temperature equations and the Stefan condition, consider the bounded subset $K_R \subset U_{ad}$ defined by

$$K_R := \left\{ h \in U_{ad} : \|h'\|_{L^2(0,t_f)} \le R \right\},$$

where $R > 0$. The embedding $H^1(0, t_f) \hookrightarrow C([0, t_f])$ implies that K_R is a nonempty, closed, convex, and bounded subset of $C([0, t_f])$ [38]. Motivated by the Stefan condition Eq. (9), we introduce the interface update operator Φ on K_R by

$$(\Phi h)(t) := h_0 + \frac{1}{\rho_i L_f} \int_0^t (F_c(h)(\tau) - F_w(\tau)) d\tau, \quad t \in [0, t_f].$$

The coupled problem is equivalent to the fixed-point equation $h = \Phi h$.

Theorem 2.4 (Self-mapping, continuity, and compactness of Φ)**.** *Assume that there exists a constant $C_R > 0$ such that $\|F_c(h)\|_{L^2(0,t_f)} \le C_R$ for all $h \in K_R$. Assume, in addition, that $h_n \to h$ in $C([0, t_f])$ implies $F_c(h_n) \to F_c(h)$ in $L^2(0, t_f)$. In particular, F_c is continuous with respect to the interface function h. Define*

$$R_0 := \frac{C_R + \|F_w\|_{L^2(0,t_f)}}{\rho_i L_f}, \quad \delta_{t_f} := \frac{\sqrt{t_f}}{\rho_i L_f}(C_R + \|F_w\|_{L^2(0,t_f)}),$$

and set $d_0 := \min\{h_0 - h_{min}, h_{max} - h_0\} > 0$. If $R \ge R_0$ and $\delta_{t_f} \le d_0$, then the operator Φ satisfies the following properties: (i) $\Phi(K_R) \subset K_R$; (ii) $\Phi : K_R \to C([0, t_f])$ is continuous; and (iii) $\Phi : K_R \to C([0, t_f])$ is compact.

Proof. (i) Fix $h \in K_R$. By definition, $(\Phi h)'(t) = \frac{1}{\rho_i L_f}(F_c(h)(t) - F_w(t))$, hence

$$\|(\Phi h)'\|_{L^2(0,t_f)} \le \frac{1}{\rho_i L_f}(\|F_c(h)\|_{L^2(0,t_f)} + \|F_w\|_{L^2(0,t_f)}) \le R_0 \le R.$$

Moreover, by the Cauchy-Schwarz inequality, for any $t \in [0, t_f]$,

$$|(\Phi h)(t) - h_0| \le \frac{1}{\rho_i L_f} \int_0^t |F_c(h) - F_w| d\tau \le \frac{\sqrt{t_f}}{\rho_i L_f} \|F_c(h) - F_w\|_{L^2(0,t_f)} \le \delta_{t_f}.$$

Therefore, $h_0 - \delta_{t_f} \le (\Phi h)(t) \le h_0 + \delta_{t_f}$. Since $\delta_{t_f} \le d_0$, it follows that

$$h_{\min} \le (\Phi h)(t) \le h_{\max}, \quad \forall t \in [0, t_f],$$

and also $(\Phi h)(0) = h_0$. Hence, $\Phi h \in K_R$, which proves $\Phi(K_R) \subset K_R$.

(ii) Let $h_n \to h$ in $C([0, t_f])$. Then, for any $t \in [0, t_f]$,

$$(\Phi h_n)(t) - (\Phi h)(t) = \frac{1}{\rho_i L_f} \int_0^t (F_c(h_n) - F_c(h)) d\tau,$$

thus

$$\|\Phi h_n - \Phi h\|_{C([0,t_f])} \le \frac{\sqrt{t_f}}{\rho_i L_f} \|F_c(h_n) - F_c(h)\|_{L^2(0,t_f)} \to 0,$$

so Φ is continuous.

(iii) The estimate in (i) shows that $\|(\Phi h)'\|_{L^2}$ is uniformly bounded, and $(\Phi h)(0) = h_0$ fixes the initial value. Hence, $\Phi(K_R)$ is bounded in $H^1(0, t_f)$. The compact embedding $H^1(0, t_f) \hookrightarrow C([0, t_f])$ implies that $\Phi(K_R)$ is relatively compact in $C([0, t_f])$. Therefore, Φ is a compact operator from K_R into $C([0, t_f])$. □

Theorem 2.5 (Existence of a solution to the coupled system)**.** *Under the assumption of Theorem 2.4, there exists $h^* \in K_R$ such that $h^* = \Phi h^*$. Let $(T_i(\cdot, \cdot; h^*), T_w(\cdot, \cdot; h^*))$ be the corresponding weak solution of the two-phase temperature system associated with the interface trajectory h^*. Then the triple (T_i, T_w, h^*) solves the fully coupled problem consisting of the two-phase heat equations, the interface conditions, and the Stefan condition.*

Proof. The set K_R is nonempty, closed, convex, and bounded in $C([0, t_f])$. Moreover, $\Phi : K_R \to K_R$ is continuous and compact. The Schauder fixed-point theorem [42] therefore yields a fixed point $h^* \in K_R$, satisfying

$$\Phi h^* = h^*.$$

Substituting h^* into the definition of Φ gives the Stefan condition. □

2.3. Physics-informed neural network

Building on the continuous model, the weak solution existence results, and the existence of a minimizer for the interface identification problem established in the previous sections, we develop a theoretical framework for using PINNs to solve the coupled ice-water two-phase system. Although these mathematical results do not prescribe a specific network architecture or training algorithm, they define the continuous target and its constraint structure and provide the basis for constructing the loss functional. Specifically, for any admissible interface trajectory $h \in U_{ad}$, well-posedness of the weak solution and uniform energy estimates ensure stability of the forward problem. This establishes a well-defined continuous target for a residual-based minimization that is built on the PDE and boundary residuals.

Strong continuity of the solution operator $\mathcal{S}$ with the respect to h further implies that convergence of interface approximations in $C([0, t_f])$ yields convergence of the predicted temperature fields. This provides theoretical support for the joint parameterization (T_θ, h_β). In addition, the construction of U_{ad} and the bounded subset K_R highlight the need to prevent domain degeneration and to suppress interface oscillations. In the numerical implementation, this corresponds to enforcing interval and initial-value constraints on the interface network, together with regularization.

Within the PINN framework, the free-boundary ice-water two-phase heat conduction system in Eqs. (1)–(3) is cast as a PDE-constrained interface identification problem, in which the unknown boundary $h(t)$ is approximated by a learnable function $h_\beta(t)$. To ensure that the interface trajectory remains within the asmissible range and to prevent domain degeneration during training, the interface output is constrained to the physical thickness interval $[h_{\min}, h_{\max}]$ through a bounded mapping. Specifically, time is first normalized to the unit interval,

$$\bar{t} = \frac{t - t_{\min}}{t_{\max} - t_{\min}}.$$

Let $N_\beta(t)$ denote the output of the interface network. The predicted interface trajectory is then defined by a sigmoid map,

$$h_\beta(t) = h_{\min} + (h_{\max} - h_{\min})\sigma(N_\beta(t)),$$

which guarantees $h_\beta(t) \in [h_{\min}, h_{\max}]$ for all t. Because the Stefan closure condition Eq. (9) couples the temperature gradients and the interface velocity at the boundary, the temperature fields and the interface trajectory must be placed within the same differentiable computational graph so that the heat flux and velocity terms remain consistent under automatic differentiation. Accordingly, we adopt a joint parameterization with a temperature network T_θ and an interface network h_β, and use residual minimization to approximate the two-phase heat equations, the outer boundary conditions, the interfacial temperature continuity condition, and the Stefan condition simultaneously. Because the system includes the ice temperature T_i and the water temperature T_w, using two independent networks can make it difficult to control derivative consistency near the interface, which in turn undermines stable enforcement of the interfacial heat flux condition. A single fully connected network T_θ is therefore used to represent both phases. It takes (z, t) as input and outputs two components, $T_\theta^{(1)}(z, t)$ and $T_\theta^{(2)}(z, t)$, written as

$$T_\theta(z, t) = T_\theta^{(1)}(z, t)\mathbf{1}_{(0,h_\beta(t))}(z) + T_\theta^{(2)}(z, t)\mathbf{1}_{(h_\beta(t),L)}(z).$$

Similarly, the observed temperature field can be written as

$$T_{\text{Obs}}(z, t) = T_{\text{Obs}}^{(1)}(z, t)\mathbf{1}_{(0,h(t))}(z) + T_{\text{Obs}}^{(2)}(z, t)\mathbf{1}_{(h(t),L)}(z).$$

The parameters θ and β are learned jointly by minimizing a weighted mean-square loss. The total loss function is defined by

$$\begin{aligned}\mathcal{L}(\theta, \beta) &= \sum_{k=1}^{2}\left[\lambda_r \mathcal{L}_r^{(k)}(\theta) + \lambda_{u_{bc}}\mathcal{L}_{u_{bc}}^{(k)}(\theta) + \lambda_{h_{bc}}\mathcal{L}_{h_{bc}}^{(k)}(\theta, \beta)\right] + \lambda_{h_{Nc}}\mathcal{L}_{h_{Nc}}(\theta, \beta) \\ &+ \lambda_{h_0}\mathcal{L}_{h_0}(\beta) + \lambda_{\text{data1}}\mathcal{L}_T(\theta) + \lambda_{\text{data2}}\mathcal{L}_h(\beta),\end{aligned}$$

where λ is nonnegative weight. Here, $\mathcal{L}_r^{(k)}$ is governing equation residual, $\mathcal{L}_{u_{bc}}^{(k)}$ enforces the outer boundary conditions, $\mathcal{L}_{h_{bc}}^{(k)}$ enforces the interfacial temperature condition, and $\mathcal{L}_{h_{Nc}}$ penalizes the Stefan

condition. $\mathcal{L}_{h_0}$ imposes the initial constraint on the interface, and $\mathcal{L}_T$ and $\mathcal{L}_h$ are the observation fitting terms for temperature and thickness, respectively. The discrete forms of these loss terms are defined as

$$\mathcal{L}_r^{(k)}(\theta) = \frac{1}{N}\sum_{i=1}^{N}\left|\rho_\ell c_\ell \partial_t T_\theta^{(k)}(z^i,t^i) - \partial_z(k_\ell \partial_z T_\theta^{(k)}(z^i,t^i)) - q_\ell(z^i,t^i)\right|^2, \tag{13a}$$

$$\mathcal{L}_{u_{bc}}^{(1)}(\theta) = \frac{1}{N}\sum_{i=1}^{N}\left|T_\theta^{(1)}(0,t^i) - T_{sfc}(t^i)\right|^2, \tag{13b}$$

$$\mathcal{L}_{u_{bc}}^{(2)}(\theta) = \frac{1}{N}\sum_{i=1}^{N}\left|T_\theta^{(2)}(L,t^i) - T_b(t^i)\right|^2, \tag{13c}$$

$$\mathcal{L}_{h_{bc}}^{(k)}(\theta,\beta) = \frac{1}{N}\sum_{i=1}^{N}\left|T_\theta^{(k)}(h_\beta(t^i),t^i) - T_f(t^i)\right|^2, \tag{13d}$$

$$\mathcal{L}_{h_{Nc}}(\theta,\beta) = \frac{1}{N}\sum_{i=1}^{N}\left|\rho_i L_f h_\beta'(t^i) - F_c(h_\beta)(t^i) + F_w(t^i)\right|^2, \tag{13e}$$

$$\mathcal{L}_{h_0}(\beta) = \frac{1}{N}\sum_{i=1}^{N}\left|h_\beta(0) - h_0\right|^2, \tag{13f}$$

$$\mathcal{L}_T(\theta) = \frac{1}{M}\sum_{i=1}^{M}\left|T_\theta(z^i,t^i) - T_{\mathrm{Obs}}(z^i,t^i)\right|^2, \tag{13g}$$

$$\mathcal{L}_h(\beta) = \frac{1}{M}\sum_{i=1}^{M}\left|h_\beta(t^i) - h_{\mathrm{Obs}}(t^i)\right|^2. \tag{13h}$$

Here, $\ell \in \{i, w\}$, N denotes the batch size for collocation points, (z^i, t^i) denotes randomly sampled points in the space-time domain, and M is the number of observational data points. The loss functional above can be viewed as an empirical discretization of the continuous constrained minimization problem. Specifically, $\mathcal{L}_r^{(k)}$, $\mathcal{L}_{u_{bc}}^{(k)}$, $\mathcal{L}_{h_{bc}}^{(k)}$, and $\mathcal{L}_{h_{Nc}}$ correspond to the PDE constraints and interfacial closure conditions of the coupled system in Section 2.1. $\mathcal{L}_T$ and $\mathcal{L}_h$ correspond to the data fitting terms in the identification model in Section 2.2. $\mathcal{L}_{h_0}$ and the interface regularization constraints reflect the stability requirements encoded in the admissible set U_{ad}. Accordingly, the total PINN loss is not a simple ad hoc sum of penalty terms, but a unified discrete approximation of a well-posed forward problem coupled to a regularized identification problem.

Because thermophysical properties such as thermal conductivity k, specific heat c, and density ρ typically jump across the ice-water interface, forcing the two-phase system into a single global residual by smoothly extending the coefficients often introduces nonphysical transition layers. It can also generate spurious derivative terms under automatic differentiation that are inconsistent with the interfacial jump structure. To remain consistent with the weak formulation in Section 2.1, we adopt a split enforcement strategy with subdomain residuals and separate interfacial conditions [34]. Specifically, the governing equation residuals are constructed separately in the ice and water subdomains

$$\mathcal{R}_i = \partial_t T_i^\theta - \partial_z(k_i \partial_z T_i^\theta) - q_i, \qquad z < h_\beta(t), \tag{14a}$$

$$\mathcal{R}_w = \partial_t T_w^\theta - \partial_z(k_w \partial_z T_w^\theta) - q_w, \qquad z > h_\beta(t), \tag{14b}$$

and coupling is imposed at $z = h_\beta(t)$ through the temperature continuity condition Eq. (13d) and the Stefan flux balance condition Eq. (13e). It is important to note that, in the numerical implementation, the Stefan flux balance condition Eq. (13e) is not enforced by invoking $F_c(h)$ only as a symbolic quantity. Instead, the interface velocity and the ice-side conductive flux are computed explicitly at moving interface collocation points. Specifically, for interface sampling times $\{t_j\}_{j=1}^{N_t}$, the interface point are $(z_j, t_j) = (h_\beta(t_j), t_j)$. Automatic differentiation is used to evaluate the interface velocity $h'_\beta = \partial_t h_\beta(t)$. The one-side derivative $\partial_z T_\theta^{(1)}(h_\beta(t_j), t_j)$ is computed from the ice branch $T_\theta^{(1)}$, yielding the ice-side conductive flux

$$F_c(h_\beta(t_j)) = -k_i \partial_z T_\theta^{(1)}(h_\beta(t_j), t_j).$$

Accordingly, the discrete Stefan residual is defined as

$$\mathcal{L}_{h_{N_c}} = \frac{1}{N_t} \sum_{j=1}^{N_t} \left| \rho L_f h'_\beta(t_j) - F_c(h_\beta)(t_j) + F_w(t_j) \right|^2 .$$

Finally, the coupled ice–water system exhibits pronounced spatial and temporal scale disparities, so training the network in the original coordinates may yield large initial losses and unstable convergence. To alleviate this issue, the spatial and temporal inputs are standardized before being fed into the network. Let (μ_z, μ_t) and (σ_z, σ_t) denote the mean and standard deviation estimated from uniformly sampled points in the domain. The following transformations are applied before the input layer:

$$f(z) = \frac{z - \mu_z}{\sigma_z}, \quad f(t) = \frac{z - \mu_t}{\sigma_t}.$$

This fixed standardization layer is embedded as part of the network architecture to reduce scale imbalance and improve training stability and convergence. The resulting PINN framework for the free-boundary ice-water two-phase system is shown in Figure 2.

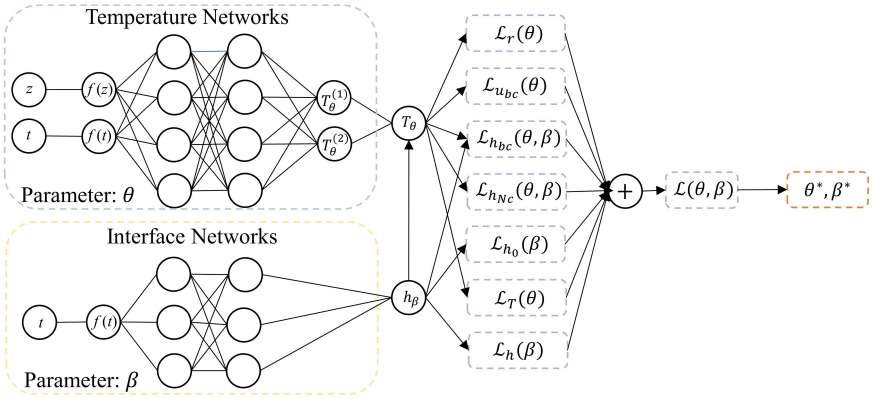

Figure 2. PINN solution of the free-boundary ice-water two-phase coupled system and the network architecture for interface identification.

3. Results

The observational dataset used in this study is collected from the Snow and Ice Mass Balance Array (SIMBA) buoy T74 deployed during the Arctic MOSAiC expedition. The buoy records the ice-water

temperature distribution, and the temporal evolution of ice thickness is inferred from the heater response measurements. The temperature chain extends from the ice surface into the underlying water column and consists of 131 temperature sensors. The vertical sensor spacing is 2 cm, and ambient temperatures are sampled automatically at 6 h intervals. Buoy T74 operated from 6 April to 26 July 2020. Sea ice thermodynamics during the melt season are influenced by multiple processes, including basal ablation and surface melt driven by atmospheric radiative forcing. Such conditions are strongly non-stationary and highly nonlinear, which can complicate model-based analysis. To reduce the impact of these effects, we focus on the ice growth period. Accordingly, the prediction interval was selected as 6 April to 6 June 2020, when the initial ice thickness was approximately 170 cm. During this period, the ice surface was covered by snow. The high snow albedo reflected most of the incident solar radiation, so the net radiative heat input at the ice surface was approximately negligible. Accordingly, the source term in the ice-ocean two-phase heat conduction model is set to $q(z,t) = 0$ W m^{-2}. The PINN is implemented and trained in TensorFlow. Full connected architectures are adopted for the temperature network and the moving interface network, with width-depth configurations of (128, 5) and (64, 4), respectively.

3.1. Single-phase sea ice heat conduction model

The complete ice-water two-phase heat conduction process involves the heat conduction within the ice, phase change, and energy exchange across the ice-water interface. However, explicitly resolving the temperature fields in both phases and their coupling substantially increases model complexity and makes parameter estimation more challenging. In practice, the ice temperature typically exhibits pronounced vertical variability, while the water temperature gradient is small and can be treated as nearly uniform. Under such conditions, the dominant influence of the ocean on the ice can be represented through the oceanic heat flux at the ice base. To reduce the complexity of the coupled two-phase formulation and to assess the feasibility of PINNs for sea ice thermodynamic modeling, the water phase is simplified in this section. The water temperature is assumed to be vertically uniform and equal to the freezing temperature, $T_w \approx T_f$. Following [43], the oceanic heat flux F_w is prescribed as a piecewise constant function of time. This simplification yields a single-phase sea ice heat conduction model, which is used as a verification setting.

To reduce the propagation of bias in F_w to interface evolution through Stefan coupling, and given that effective conductive behavior at the interface is jointly influenced by sea-ice microstructure, salinity evolution, air bubbles and brine distribution, and boundary condition uncertainty [44], a multiplicative correction factor γ is introduced into the ice-side conductive flux. This choice follows the treatment of low-dimensional physical correction parameters and constrained identification in [45]. Specifically, the ice-side conductive flux $F_c(h)(t)$ in the Stefan condition Eq. (9) is corrected multiplicatively, and the coupling constraint is enforced in residual form as

$$\rho_i L_f h'(t) - \gamma F_c(h)(t) + F_w(t) = 0.$$

To ensure physical admissibility of γ and avoid degeneracy in the identification, a reparameterization with an interval constraint is adopted,

$$\gamma = \gamma_{\min} + (\gamma_{\max} - \gamma_{\min})\,\sigma(\gamma_{\text{raw}}) \in [\gamma_{\min}, \gamma_{\max}],$$

where $\sigma(\cdot)$ is the sigmoid function. In addition, a log-prior regularization term $\mathcal{R}_\gamma = \left|\log \gamma\right|^2$ is introduced to penalize nonphysical departures of γ from the baseline scale. This treatment effectively restricts identification of the interfacial flux correction parameter to a bounded admissible set, implementing a constrained identification consistent with the admissible set concept in the minimization problem of Section 2.2 within the differentiable PINN optimization framework.

To mitigate the nonconvex optimization instability induced by Stefan free-boundary coupling, a three-stage training strategy is adopted. This strategy does not alter the underlying constrained minimization problem. Instead, during the parameterized approximation, it progressively releases degrees of freedom and shifts the dominant loss terms, first learning the main structure of the temperature field, then enforcing closure of the interface dynamics, and finally refining the interface trajectory. This staged schedule constructs a more stable optimization pathway [46]. The motivation can be understood from the sensitivity structure of the Stefan interface residual. Let

$$R_\Gamma(t) = \rho L_f h'_\beta(t) - \gamma F_c(h_\beta)(t) + F_w(t).$$

A formal first-order perturbation then satisfies

$$\delta R_\Gamma \approx \rho_i L_f \delta h'_\beta - \gamma\big(\partial_h F_c(h_\beta)\delta h_\beta + D_T F_c(h_\beta)[\delta T]\big) - F_c(h_\beta)\delta\gamma.$$

This expression shows that the interface residual depends jointly on perturbations in the interface trajectory δh_β, the temperature field δT, and the flux correction parameter $\delta\gamma$. If (θ, β, γ) are all updated aggressively at early training stages, gradients from the thickness and interface losses can be amplified through the term $D_T F_c(h_\beta)[\delta T]$, which may trigger short-time, nonphysical oscillations in $h_\beta(t)$. The three-stage strategy is implemented as follows:

- **Stage 0 (learning the main temperature structure):**
  Training is driven mostly by the PDE residuals, the outer boundary constraints, and the temperature observation fitting. The temperature network parameters θ are updated first, while the interface trajectory terms and the Stefan interface loss are assigned relatively small weights. The aim is to establish the dominant structure of the temperature field and its major gradient patterns, preventing the interface network from absorbing local temperature errors too early.
- **Stage 1 (closing the interface dynamics):**
  Once the main temperature structure is established, the weights on $\mathcal{L}_{h_{N_c}}$ and $\mathcal{L}_h$ are increased and β and γ are optimized jointly. This stage uses the established temperature gradient structure to transmit Stefan flux information to the interface evolution in a more stable manner.
- **Stage 2 (fine trajectory correction):**
  The major temperature network parameters are frozen at θ_f, and only a small set of final-layer parameters θ_l, together with (β, γ), remain trainable. The weights on $\mathcal{L}_{h_{N_c}}$ and $\mathcal{L}_h$ further increase. This stage preserves the globally smooth temperature structure and suppresses high-frequency perturbations arising from backpropagation through $D_T F_c(h_\beta)[\delta T]$. Late-stage corrections therefore rely mostly on low-dimensional adjustments in (β, γ) while retaining limited capacity to refine the temperature profile near the interface.

In summary, the three-stage training strategy is designed to alleviate gradient competition and scale imbalance in the coupled optimization, rather than to modify the continuous model or the underlying constrained minimization structure. The trainable parameter sets, loss-term weights, and learning rates for the three stages are summarized in Table 1. Using the trained PINN, the predicted spatiotemporal evolution of the sea ice temperature field and the interface position (ice thickness) over the test period, together with comparisons against the corresponding observations, are shown in Figure 3.

Table 1. Three-stage optimization with partial unfreezing strategy in single-phase heat conduction model.

Stage	Trainable params	Epochs	Optimizer & LR	LR scheduler	Objective (weights)
0	θ, freeze β, γ	3000	Adam, lr = 3×10^{-4}	CosineAnnealing, $\eta_{\min} = 10^{-5}$	$\mathcal{L}_0 = 800\mathcal{L}_{u_{bc}} + 50\mathcal{L}_T$
1	θ, β, γ	20000	Adam, lr = 3×10^{-4}	CosineAnnealing, $\eta_{\min} = 10^{-5}$	$\mathcal{L}_1 = 100\mathcal{L}_r + 500\mathcal{L}_{u_{bc}} + \lambda_{h_{bc}}(n)\mathcal{L}_{h_{bc}} + 60\mathcal{L}_{h_{Nc}} + 20\mathcal{L}_T + 50\mathcal{L}_h + 200\mathcal{L}_{h_0} + 2\mathcal{R}_\gamma$ Ramp: $\lambda_{h_{bc}}(n)$ from 10^3 to 2×10^4 ($N_{\text{ramp}} = 6000$)
2	β, γ, θ_l (last 2 linear layers of temp net), freeze θ_f	20000	Adam, param groups: $\text{lr}_{\beta,\gamma} = 5 \times 10^{-5}$ $\text{lr}_{\theta_l} = 10^{-5}$	CosineAnnealing, $\eta_{\min} = 5 \times 10^{-6}$	$\mathcal{L}_2 = 8000\mathcal{L}_h + 2 \times 10^4\mathcal{L}_{h_{bc}} + 1200\mathcal{L}_{h_{Nc}} + 500\mathcal{L}_{h_0} + 0.2\mathcal{R}_\gamma + 5\mathcal{L}_T + 50\mathcal{L}_{u_{bc}}$

Figures 3a–c show that the PINN reproduces the temperature field agree closely with the observations ($R^2 = 0.99$). The overall error remains below 0.5 °C (RMSE = 0.44 °C, MAE = 0.32 °C), with only minor local discrepancies. As seen by comparing Figures 3a and 3b, the observed isotherms exhibit weak, approximately linear fluctuations, whereas the PINN prediction is smoother. In particular, the −8 °C isotherm is slightly elevated relative to the observations. This behavior is likely related to the smoothing effect introduced during Stages 0–1, which encourages the temperature network to fit the domain large-scale structure and can attenuate small-scale fluctuations. Figure 3c further confirms that prediction errors are below 0.5 °C over most of the domain, approaching 1 °C only in a few regions. The bias show a clear vertical pattern: A weak warm bias in the mid-depth ice and a cold bias near both the surface and the base. This distribution is likely linked to the relatively strong boundary enforcement, which constrains the near-boundary gradients, while the interior temperature profile is governed primarily by internal heat conduction governed by the heat equation. Figures 3d and 3e show that the learned ice thickness evolution also matches the observations well ($R^2 = 0.93$), with thickness differences remaining below 2.5 cm. The Stage 2 refinement of the interface network captures the overall thickening trend effectively, but the response to short-term thickness fluctuations remains weaker. This is likely because freezing most of the temperature network in Stage 2 preserves a globally smooth temperature structure during the dynamic evolution, which suppresses small-scale transient variations in $h(t)$.

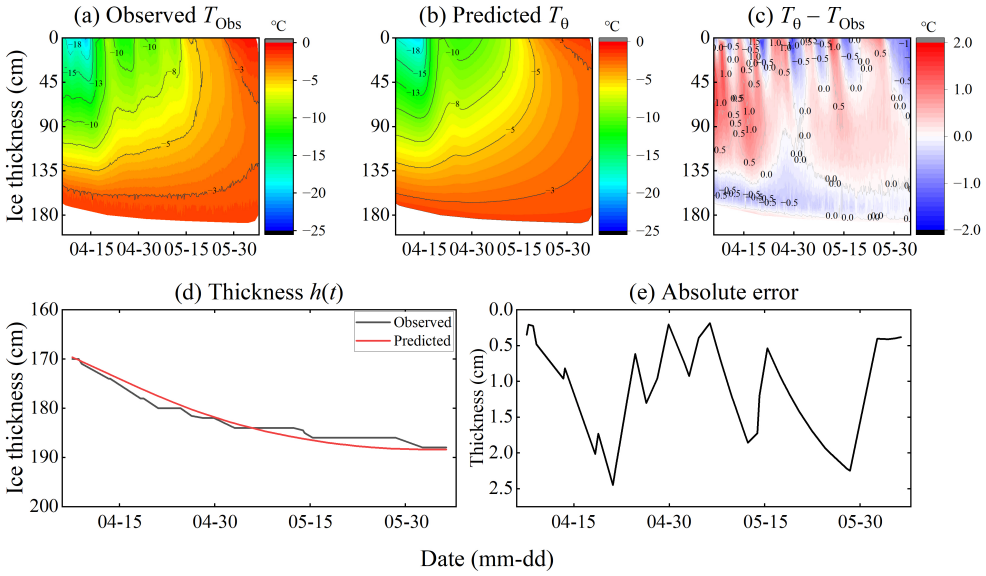

Figure 3. Comparison between PINN predictions and observations in single-phase heat conduction model. (a) Observed temperature field (T_{Obs}). (b) PINN-predicted temperature field (T_{θ}). (c) Temperature prediction error ($T_{\theta} - T_{\mathrm{Obs}}$). (d) Predicted and observed ice thickness evolution. (e) Absolute error of the ice thickness prediction.

3.2. Two-phase heat conduction model for the ice-ocean system

Compared with single-phase sea-ice heat conduction, the ice-water two-phase model requires explicit prediction of ice and water temperature fields on a spatial domain that evolves with the interface. Because the Stefan condition couples the interfacial fluxes and interface motion in a strongly nonlinear manner, the interface region is more sensitive to observation and boundary errors. During training, this sensitivity can induce gradient competition among residual terms and leads to interface drift. To reduce the dependence on delicate loss weighting under multiple boundary and interfacial constraints, and to stabilize enforcement of the interfacial closure during optimization, two additional components are introduced on top of the single-phase training strategy. These are hard-constraint embedded representations and an observation-driven stable interface boundary, which together improve convergence stability and identifiability for the strongly coupled two-phase PDE Stefan inverse problem.

First, to avoid strong sensitivity to loss weights when outer boundary conditions and interfacial temperature conditions enter the objective only through soft penalties, and to reduce competition between boundary and PDE residuals, the temperature boundary conditions are embedded directly into the parameterized representations of the ice and water temperature fields. The constraints are therefore satisfied exactly at the level of the function representation, rather than being approximated through penalty terms. This is a standard hard-constraint treatment in PINNs, in which structured trial functions or distance-function constructions restrict the search space to an admissible function class that already satisfies the boundary constraints. Such exact enforcement has been shown to improve training stability and accuracy and to reduce reliance on boundary penalty tuning [47]. Specifically, normalized coordinates are introduced,

$$\alpha(z,t) = \Pi_{[0,1]}\left(\frac{z}{h(t)}\right), \quad \zeta(z,t) = \Pi_{[0,1]}\left(\frac{z-h(t)}{L-h(t)}\right),$$

where $\Pi_{[0,1]}$ is the projection operator. With shape-correction networks $N_i(z,t)$ and $N_w(z,t)$, the temperature fields are constructed as

$$T_i(z,t) = T_{\mathrm{sfc}}(t) + \alpha(z,t)\big(T_{\mathrm{f}}(t) - T_{\mathrm{sfc}}(t)\big) + z\big(1-\alpha(z,t)\big)N_i(z,t),$$

$$T_w(z,t) = T_{\mathrm{f}}(t) + \zeta(z,t)\big(T_{\mathrm{b}}(t) - T_{\mathrm{f}}(t)\big) + \big(z-h(t)\big)\big(1-\zeta(z,t)\big)N_w(z,t).$$

By construction,

$$T_i(0,t) = T_{\mathrm{sfc}}(t),\ T_i(h(t),t) = T_w(h(t),t) = T_f(t),\ T_w(L,t) = T_b(t),$$

so the outer boundary temperature conditions and interfacial temperature continuity hold for any network parameters, and no additional penalty terms are required for these constraints. The projection operator $\Pi_{[0,1]}$ is introduced for numerical robustness. For collocation points sampled within the physical subdomain, α and ζ lie in $[0,1]$, so the projection does not alter the definition of the interior residuals. Here, $\alpha(z,t)$ and $\zeta(z,t)$ act as local normalized coordinates that define linear interpolation bases, satisfying the endpoint temperature constraints. The multiplicative factors $z(1-\alpha)$ and $(z-h_\beta(t))(1-\zeta)$ ensure that the correction networks N_i and N_w do not modify the embedded boundary and interface values. Training can therefore focus on learning the interior temperature profiles and their dynamics, rather than repeatedly correcting boundary errors, which reduces sensitivity to boundary loss weights. This construction aligns with the affine lifting and boundary homogenization ideas introduced in Section 2; namely, enforce known constraints explicitly and parameterize only the remaining degrees of freedom.

Building on this construction, the interfacial temperature $T_f(t)$ is specified in an observation-driven manner to further suppress undue amplification of local observation bias by the interfacial closure. Specifically, the observed thickness is linearly interpolated to obtain $h_{\mathrm{Obs}}(t)$. From the temperature profile, the ice-side observation closest to the interface is selected as $T_{f,\mathrm{Obs}}(t)$, and

$$T_{\mathrm{f}}(t) = T_{f,\mathrm{Obs}}(t) + \Delta T_0, \quad \Delta T_0 \in [-d_0, d_0],$$

is imposed. Here, ΔT_0 is a bounded learnable scalar that compensates for systematic bias in near-interface observations and limits nonphysical propagation of this bias into the Stefan flux closure through the interfacial temperature gradient. Let ϑ denote the learnable parameter controlling ΔT_0, and let $\mathcal{R}_{\Delta T_0}$ be a weak prior regularization term for ΔT_0. This construction can then be interpreted as a bounded low-dimensional correction built on an observation-based interface temperature. Its role is consistent with the admissible set perspective in the identification problem of Section 2. It preserves interpretability of $T_f(t)$ while enabling limited bias correction, thereby balancing stability and identifiability. The trainable parameter sets and loss weights for the three-stage training procedure of the ice-water two-phase system are summarized in Table 2. The predicted spatiotemporal evolution of the two-phase temperature field and the interface position over the testing interval, together with comparisons against observations, are shown in Figure 4.

Table 2. Three-stage optimization with a partial unfreezing strategy in a two-phase heat conduction model.

Stage	Trainable params	Epochs	Optimizer & LR	LR scheduler	Objective (weights)
0	$\theta_i, \theta_w, \vartheta$, freeze β, γ	3000	Adam, lr = 3×10^{-4}	CosineAnnealing, $\eta_{\min} = 10^{-5}$	$\mathcal{L}_0 = 1.0\mathcal{L}_T + 0.1\mathcal{R}_{\Delta T_0}$
1	$\theta_i, \theta_w, \beta, \gamma, \vartheta$	20000	Adam, lr = 3×10^{-4}	CosineAnnealing, $\eta_{\min} = 10^{-5}$	$\mathcal{L}_1 = 80\mathcal{L}_T + 10^4\mathcal{L}_h + 50\mathcal{L}_r^{(1)} + 500\mathcal{L}_r^{(2)} + 2500\mathcal{L}_{h_{Nc}} + 500\mathcal{L}_{h_0} + 5\mathcal{R}_{\Delta T_0} + 0.05\mathcal{R}_\gamma$
2	$\beta, \gamma, \theta_i, \theta_{w,\ell}, \vartheta$, freeze $\theta_{w,f}$	30000	Adam, param groups: $\mathrm{lr}_\beta = 2 \times 10^{-4}$ $\mathrm{lr}_{\text{others}} = 2 \times 10^{-5}$	CosineAnnealing, $\eta_{\min} = 5 \times 10^{-6}$	$\mathcal{L}_2 = 50\mathcal{L}_T + 1.5 \times 10^4\mathcal{L}_h + 50\mathcal{L}_r^{(1)} + 500\mathcal{L}_r^{(2)} + 3500\mathcal{L}_{h_{Nc}} + 500\mathcal{L}_{h_0} + 5\mathcal{R}_{\Delta T_0} + 0.05\mathcal{R}_\gamma + 0.05\mathcal{R}_{\gamma,s}$

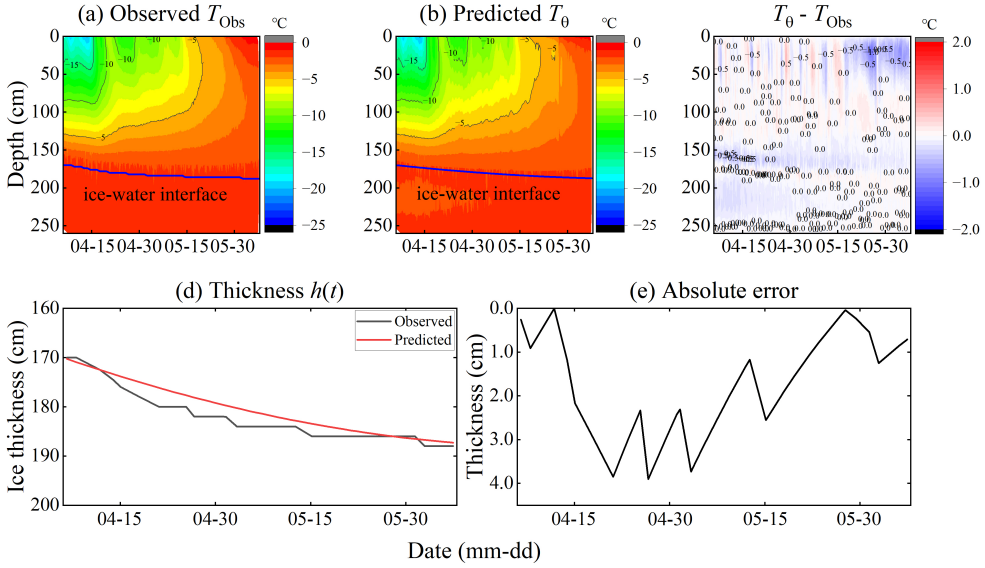

Figure 4. Comparison between PINN predictions and observations in two-phase heat conduction model. (a) Observed temperature field (T_{Obs}). (b) PINN-predicted temperature field (T_θ). (c) Temperature prediction error ($T_\theta - T_{\text{Obs}}$). (d) Predicted and observed ice thickness evolution. (e) Absolute error of the ice thickness prediction. In (a) and (b), the blue line denotes the ice-water interface.

Figure 4 shows that the PINN closely matches the observed ice and water temperature fields, capturing the conduction-dominated and its temporal evolution. In both phases, the RMSE and MAE are below 0.3 °C. Comparing Figures 4a and 4b, the model reproduces the shape of isotherms within the ice and their time evolution. It also resolves the weak-gradient layer near the ice-water interface, which helps maintain continuity of the thermal structure across the two phases. A slight cold bias appears in the water phase at early times. This bias is likely associated with uncertainty in the water-side initial

condition and boundary constraints, and it persists as a residual systematic offset under the network's smooth approximation. Figure 4c further indicates that temperature errors are close to zero over most of the space-time domain. The overall magnitude remains within 1 °C, and no systematic error growth is observed as time progresses. The interface inversion results (Figure 4d) show that the PINN-predicted ice thickness trajectory is smoother than the measurements and is slightly thinner overall. The overall RMSE and MAE of the thickness reconstruction are below 2 cm, although the absolute error reaches 3–4 cm during a few short intervals (Figure 4e). These localized deviations are consistent with short-time adjustments of the near-interface temperature gradients. Since the interface motion is driven by the flux difference across the interface, even small perturbations in the gradients can amplify into noticeable interface-position errors over short time scales. Relative to the single-phase conduction results (Figure 3), the ice-phase temperature error is slight reduced, whereas the thickness error increases. This contrast suggests that representing the ocean influence through a time-varying oceanic heat flux provides a more effective constraint on thickness evolution. This also indicates that thickness inversion is more sensitive than temperature reconstruction to interfacial flux closure and boundary specification.

4. Conclusions

In this study, we develop a Stefan-consistent physics-informed neural network for Arctic sea-ice thermodynamics under sparse observations, enabling simultaneous reconstruction of the ice–water two-phase temperature fields and inversion of the interface (ice thickness) trajectory. The formulation is supported by a weak-solution framework and coupled well-posedness results, yielding a unified modeling and training paradigm for the associated inverse problem.

Validation is performed using MOSAiC SIMBA buoy T74 data from 6 April to 6 June 2020, with an 80/20 train–test split. A progressive strategy is adopted, starting from an equivalent oceanic heat flux representation and then extending to the fully coupled two-phase system. In the equivalent-flux stage, a three-stage training strategy improves convergence, while a multiplicative conductive flux correction mitigates systematic heat flux bias. This stage achieves ice temperature RMSE = 0.44 °C and MAE = 0.32 °C, with thickness absolute error below 2.5 cm. In the fully coupled stage, hard enforcement of boundary conditions enhances physical consistency and stability, giving ice temperature RMSE = 0.21 °C and MAE = 0.15 °C, and water temperature RMSE = 0.10 °C and MAE = 0.07 °C. The inferred thickness error remains within 4 cm, indicating that thickness is more sensitive than temperature to interfacial flux closure and boundary specification.

Accordingly, we establish a unified framework for Stefan free-boundary inverse problems that integrates continuous theoretical analysis, a physics-consistent PINN implementation, and observation-driven validation. The framework provides a coordinated treatment of interface trajectory identification, interfacial flux closure, and stable solution. In this work, we focus on the sea-ice growth season. For the melt season, where coupling is stronger and nonlinearities are more pronounced, additional observational constraints and process representations will be required. A further limitation is that no quantitative comparison has been conducted, under a unified experimental setting, against conventional numerical Stefan solvers or data assimilation approaches. Therefore, in future work, we will address melt-season applicability, stability and robustness, and systematic intermethod comparisons under consistent evaluation conditions. More broadly, the framework can be extended to coupled air, snow, ice, and ocean configurations for multilayer temperature field reconstruction and thickness evolution

prediction, providing a methodological basis for cross-medium energy budget closure and full-season diagnosis of sea-ice thermodynamic evolution.

Author contributions

Yang Liu: Conceptualization, software, validation, formal analysis, data curation, writing-original draft, and visualization. **Lei Wang:** Conceptualization, formal analysis, writing-original draft, writing-review, and funding acquisition. **BingYan Gao:** Writing-review. **XueLing Yi:** Writing-review. **Peng Lu:** Writing-review and funding acquisition. **Xu Zhang:** Writing-review and funding acquisition.

Use of Generative-AI tools declaration

The authors declare that they did not utilize any artificial intelligence (AI) tools in the creation of this article.

Acknowledgments

This work was supported by grants from the National Natural Science Foundation of China (42320104004, 42576269). X.Z. was supported by the Fundamental Research Funds for the Central Universities (DUT24LK006).

Conflict of interest

All authors declare no conflicts of interest in this paper.

References

1. J. Overland, E. Dunlea, J. E. Box, R. Corell, M. Forsius, V. Kattsov, et al., The urgency of Arctic change, *Polar Sci.,* **21** (2019), 6–13. http://dx.doi.org/10.1016/j.polar.2018.11.008
2. A. G. Dai, D. H. Luo, M. R. Song, J. P. Liu, Arctic amplification is caused by sea-ice loss under increasing CO2, *Nat. Commun.,* **10** (2019), 121. http://dx.doi.org/10.1038/s41467-018-07954-9
3. D. K. Perovich, C. Polashenski, Albedo evolution of seasonal Arctic sea ice, *Geophys. Res. Lett.,* **39** (2012), L08501. http://dx.doi.org/10.1029/2012GL051432
4. R. A. Pedersen, I. Cvijanovic, P. L. Langen, B. M. Vinther, The impact of regional arctic sea ice loss on atmospheric circulation and the NAO, *J. Climate,* **29** (2016), 889–902. https://doi.org/10.1175/JCLI-D-15-0315.1
5. J. C. Stroeve, V. Kattsov, A. Barrett, M. Serreze, T. Pavlova, M. Holland, et al., Trends in Arctic sea ice extent from CMIP5, CMIP3 and observations, *Geophys. Res. Lett.,* **39** (2012), L16502. http://dx.doi.org/10.1029/2012GL052676
6. D. Notz, J. Stroeve, Observed arctic sea-ice loss directly follows anthropogenic CO2 emission, *Science,* **354** (2016), 747–750. http://dx.doi.org/10.1126/science.aag2345

7. R. Kwok, G. F. Cunningham, Contribution of melt in the Beaufort Sea to the decline in Arctic multiyear sea ice coverage: 1993–2009, *Geophys. Res. Lett.,* **37** (2010), L20501. http://dx.doi.org/10.1029/2010GL044678

8. H. Sumata, L. Steur, D. V. Divine, M. A. Granskog, S. Gerland, Regime shift in Arctic Ocean sea ice thickness, *Nature,* **615** (2023), 443–449. http://dx.doi.org/10.1038/s41586-022-05686-x

9. L. Albedyll, C. H. W. Dierking, Thermodynamic and dynamic contributions to seasonal Arctic sea ice thickness distributions from airborne observations, *Elem. Sci. Anth.,* **10** (2022), 74. http://dx.doi.org/10.1525/elementa.2021.00074

10. I. A. Raphael, D. K. Perovich, C. M. Polashenski, D. Clemens-Sewall, P. Itkin, R. Lei, et al., Sea ice mass balance during the MOSAiC drift experiment: Results from manual ice and snow thickness gauges, *Elem. Sci. Anth.,* **12** (2024), 40. http://dx.doi.org/10.1525/elementa.2023.00040

11. R. B. Lei, N. Li, P. Heil, B. Cheng, Z. H. Zhang, B. Sun, Multiyear sea-ice thermal regimes and oceanic heat flux derived from an ice mass balance buoy in the Arctic Ocean, *J. Geophys. Res. Oceans,* **119** (2014), 537–547. http://dx.doi.org/10.1002/2012JC008731

12. E. Carmack, I. Polyakov, L. Padman, I. FER, E. Hunke, J. Hutchings, et al., Toward quantifying the increasing role of oceanic heat in sea ice loss in the new arctic, *Bull. Amer. Meteor. Soc.,* **96** (2015), 2079–2105. http://dx.doi.org/10.1175/BAMS-D-13-00177.1

13. J. A. Richter-Menge, D. K. Perovich, B. C. Elder, K. Claffey, I. Rigor, M. Ortmeyer, Ice mass-balance buoys: a tool for measuring and attributing changes in the thickness of the Arctic sea-ice cover, *Ann. Glaciol.,* **44** (2006), 205–210. http://dx.doi.org/10.3189/172756406781811727

14. R. L. Tilling, A. Ridout, A. Shepherd, Estimating Arctic sea ice thickness and volume using CryoSat-2 radar altimeter data, *Adv. Space Res.,* **62** (2018), 1203–1225. http://dx.doi.org/10.1016/j.asr.2017.10.051

15. K. Jackson, J. Wilkinson, T. Maksym, D. Meldrum, J. Beckers, C. Haas, et al., A novel and low-cost sea ice mass balance buoy, *J. Atmos. Oceanic Technol.,* **30** (2013), 2676–2688. http://dx.doi.org/10.1175/JTECH-D-13-00058.1

16. R. Kwok, G. F. Cunningham, ICES at over Arctic sea ice: Estimation of snow depth and ice thickness, *J. Geophys. Res.,* **113** (2008), C08010. http://dx.doi.org/10.1029/2008JC004753

17. S. Kacimi, R. Kwok, Arctic snow depth, ice thickness, and volume from ICESat-2 and CryoSat-2: 2018–2021, *Geophys. Res. Lett.,* **49** (2022), e2021GL097448. http://dx.doi.org/10.1029/2021GL097448

18. J. C. Landy, A. A. Petty, M. Tsamados, J. C. Stroeve, Sea ice roughness overlooked as a key source of uncertainty in CryoSat-2 ice freeboard retrievals, *J. Geophys. Res. Oceans,* **125** (2020), e2019JC015820. http://dx.doi.org/10.1029/2019JC015820

19. M. Li, C. Ke, B. Cheng, J. Ma, H. Jiang, X. Shen, Inter-comparisons of Arctic snow depth products, *Int. J. Digit. Earth,* **17** (2024), 2376286. http://dx.doi.org/10.1080/17538947.2024.2376286

20. A. K. Turner, E. C. Hunke, Impacts of a mushy-layer thermodynamic approach in global sea-ice simulations using the CICE sea-ice model, *J. Geophys. Res. Oceans,* **120** (2015), 1253–1275. http://dx.doi.org/10.1002/2014JC010358

21. Y. J. Fang, T. W. Wu, A. X. Hu, M. Chu, A modified thermodynamic sea ice model and its application, *Ocean Model.,* **178** (2022), 102096. http://dx.doi.org/10.1016/j.ocemod.2022.102096

22. A. F. Roberts, E. C. Hunke, R. Allard, D. A. Bailey, A. P. Craig, J. F. Lemieux, et al., Quality control for community-based sea-ice model development, *Philos. Trans. Royal Soc. A,* **376** (2018), 20170344. http://dx.doi.org/10.1098/rsta.2017.0344

23. L. Yu, J. P. Liu, Y. Q. Gao, Q. Shu, A sensitivity study of arctic ice-ocean heat exchange to the three-equation boundary condition parametrization in CICE6, *Adv. Atmos. Sci.,* **39** (2022), 1398–1416. http://dx.doi.org/10.1007/s00376-022-1316-y

24. F. G. Gu, F. Kauker, Q. H. Yang, B. Han, Y. J. Fang, C. W. Liu, Effects of freezing temperature parameterization on simulated sea-ice thickness validated by MOSAiC observations, *Geophys. Res. Lett.,* **51** (2024), e2024GL108281. http://dx.doi.org/10.1029/2024GL108281

25. P. Nanda, G. M. M. Reddy, M. Vynnycky, Inverse two-phase nonlinear stefan and cauchy-stefan problems: A phase-wise approach, *Comput. Math. Appl.,* **123** (2022), 216–226. http://dx.doi.org/10.1016/j.camwa.2022.08.009

26. C. Ghanmi, S. Mani Aouadi, F. Triki, Recovering the initial condition in the one-phase Stefan problem, *Discrete Cont. Dyn. Syst. S,* **15** (2022), 1143–1164. http://dx.doi.org/10.3934/dcdss.2021087

27. M. Raissi, P. Perdikaris, G. E. Karniadakis, Physics-informed neural networks: A deep learning framework for solving forward and inverse problems involving nonlinear partial differential equations, *J. Comput. Phys.,* **378** (2019), 686–707. http://dx.doi.org/10.1016/j.jcp.2018.10.045

28. M. Someya, T. Furumura, Physics-informed neural networks for offshore tsunami data assimilation, *Geophys. J. Int.,* **242** (2025), ggaf243. http://dx.doi.org/10.1093/gji/ggaf243

29. M. Heinkenschloss, D. P. Kouri, Optimization problems governed by systems of PDEs with uncertainties, *Acta Numer.,* **34** (2025), 1–92. http://dx.doi.org/10.1017/S0962492925000029

30. S. Nabi, P. Grover, C. P. Caulfield, Robust preconditioned one-shot methods and direct-adjoint-looping for optimizing Reynolds-averaged turbulent flows, *Comput. Fluids,* **238** (2022), 105390. http://dx.doi.org/10.1016/j.compfluid.2022.105390

31. S. Cuomo, V. S. D. Cola, F. Giampaolo, G. Rozza, M. Raissi, F. Piccialli, Scientific machine learning through physics-informed neural networks: Where we are and what's next, *J. Sci. Comput.,* **92** (2022), 88. http://dx.doi.org/10.1007/s10915-022-01939-z

32. G. E. Karniadakis, I. G. Kevrekidis, L. Lu, P. Perdikaris, S. Wang, L. Yang, Physics-informed machine learning, *Nat. Rev. Phys.,* **3** (2021), 422–440. http://dx.doi.org/10.1038/s42254-021-00314-5

33. S. F. Wang, X. L. Yu, P. Perdikaris, When and why PINNs fail to train: A neural tangent kernel perspective, *J. Comput. Phys.,* **449** (2022), 110768. http://dx.doi.org/10.1016/j.jcp.2021.110768

34. A. D. Jagtap, E. Kharazmi, G. E. Karniadakis, Conservative physics-informed neural networks on discrete domains for conservation laws: Applications to forward and inverse problems, *Comput. Methods Appl. Mech. Eng.,* **365** (2020), 113028. http://dx.doi.org/10.1016/j.cma.2020.113028

35. S. Berrone, C. Canuto, M. Pintore, N. Sukumar, Enforcing Dirichlet boundary conditions in physics-informed neural networks and variational physics-informed neural networks, *Heliyon,* **9** (2023), e18820. http://dx.doi.org/10.1016/j.heliyon.2023.e18820

36. T. M. Yang, Z. H. Qian, N. Z. Hang, M. B. Liu, S-PINN: Stabilized physics-informed neural networks for alleviating barriers between multi-level co-optimization, *Comput. Methods Appl. Mech. Eng.,* **447** (2025), 118348. http://dx.doi.org/10.1016/j.cma.2025.118348

37. S. F. Wang, P. Perdikaris, Deep learning of free boundary and Stefan problems, *J. Comput. Phys.,* **428** (2021), 109914. http://dx.doi.org/10.1016/j.jcp.2020.109914

38. H. Brezis, *Functional analysis, sobolev spaces and partial differential equations*, Springer, 2011. http://dx.doi.org/10.1007/978-0-387-70914-7

39. J. L. Lions, E. Magenes, *Non-homogeneous boundary value problems and applications*, Springer, 1972. http://dx.doi.org/10.1007/978-3-642-65161-8

40. W. Lv, E. Feng, Z. J. Li, A coupled thermodynamic system of sea ice and its parameter identification, *Appl. Math. Model.,* **32** (2008), 1198–1207. http://dx.doi.org/10.1016/j.apm.2007.03.006

41. B. Dacorogna, *Direct methods in the calculus of variations*, Springer, 2008. http://dx.doi.org/10.1007/978-0-387-55249-1

42. A. Granas, J. Dugundji, *Fixed point theory*, Springer, 2003. http://dx.doi.org/10.1007/978-0-387-21593-8

43. R. B. Lei, M. Hoppmann, B. Cheng, G. Y. Zuo, J. Zhao, L. Lin, et al., Seasonality and timing of sea ice mass balance and heat fluxes in the Arctic transpolar drift during 2019–2020, *Elem. Sci. Anth.,* **10** (2022), 89. http://dx.doi.org/10.1525/elementa.2021.000089

44. D. J. Pringle, H. Eicken, H. J. Trodahl, L. G. E. Backstrom, Thermal conductivity of landfast Antarctic and Arctic sea ice, *J. Geophys. Res.,* **112** (2007), C04017. http://dx.doi.org/10.1029/2006JC003641

45. A. M. Tartakovsky, C. O. Marrero, P. Perdikaris, G. D. Tartakovsky, D. Barajas-Solano, Physics-informed deep neural networks for learning parameters and constitutive relationships in subsurface flow problems, *Water Resour. Res.,* **56** (2020), e2019WR026731. http://dx.doi.org/10.1029/2019WR026731

46. S. F. Wang, Y. J. Teng, P. Perdikaris, Understanding and mitigating gradient flow pathologies in physics-informed neural networks, *SIAM J. Sci. Comput.,* **43** (2021), A3055–A3081. http://dx.doi.org/10.1137/20M1318043

47. N. Sukumar, A. Srivastava, Exact imposition of boundary conditions with distance functions in physics-informed deep neural networks, *Comput. Methods Appl. Mech. Eng.,* **389** (2022), 114333. http://dx.doi.org/10.1016/j.cma.2021.114333

AIMS Press

© 2026 the Author(s), licensee AIMS Press. This is an open access article distributed under the terms of the Creative Commons Attribution License (https://creativecommons.org/licenses/by/4.0)